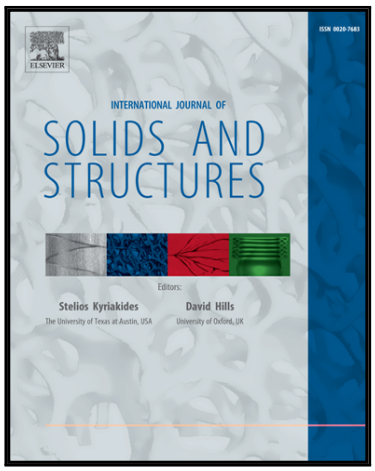

Wrinkling of Transversely Loaded Spinning Membranes

Mélanie Delapierre, Debadi Chakraborty, John E. Sader, Sergio Pellegrino

PII: S0020-7683(18)30033-7
DOI: 10.1016/j.ijsolstr.2018.01.031
Reference: SAS 9880

To appear in: *International Journal of Solids and Structures*

Received date: 23 July 2017
Revised date: 7 January 2018
Accepted date: 24 January 2018

Please cite this article as: Mélanie Delapierre, Debadi Chakraborty, John E. Sader, Sergio Pellegrino, Wrinkling of Transversely Loaded Spinning Membranes, *International Journal of Solids and Structures* (2018), doi: 10.1016/j.ijsolstr.2018.01.031

Wrinkling of Transversely Loaded Spinning Membranes

Mélanie Delapierre[a], Debadi Chakraborty[b], John E. Sader[b,c], Sergio Pellegrino[a,*]

[a] *Graduate Aerospace Laboratories, California Institute of Technology, 1200 E California Blvd, Pasadena, CA 91125*
[b] *University of Melbourne, Parkville VIC 3010, Australia*
[c] *Department of Physics, California Institute of Technology, Pasadena, CA 91125*

Abstract

Spinning membrane structures provide a mass-efficient solution for large space apertures. This paper presents a detailed study of the wrinkling of spinning circular membranes loaded by transverse, uniform loads. Experimental measurements of the angular velocities at which different membranes become wrinkled, and of the wrinkling mode transitions that occur upon spin down of the membrane, are presented. A theoretical formulation of the problem is presented, from which pairs of critical angular velocities and critical transverse loads are determined. A general stability chart is presented, which identifies the stability limits in terms of only two dimensionless parameters, for any membrane. The transition between bending dominated behavior and in-plane dominated behavior is identified, and it is shown that in the bending-dominated case the critical non-dimensional transverse load is independent from the non-dimensional angular velocity.

Keywords: buckling, wrinkled membranes, von Kármán plate theory, nonlinear dynamical systems

*Corresponding author
Email addresses: melanie.delapierre@caltech.edu (Mélanie Delapierre), debadi.chakraborty@unimelb.edu.au (Debadi Chakraborty), jsader@unimelb.edu.au (John E. Sader), sergiop@caltech.edu (Sergio Pellegrino)

1. Introduction

Membranes are widely used in deployable space structures, as they allow tight packaging for launch. Their low bending stiffness, which is advantageous for efficient packaging, requires that the deployed shape is stabilized by applying a state of prestress. This is often done by applying edge forces through a set of deployable booms (as in the James Webb sunshield (Clampin, 2008)). A lighter and potentially simpler way of prestressing the membrane is by means of centrifugal forces. It was recently demonstrated in the IKAROS solar sail (Sawada et al., 2007), although unexpected shape deviations were observed (Satou et al., 2015). Spinning membranes are also of interest for future, ultralight space-based solar power satellites. Both solar sails and solar power satellites require ultralight structures that can remain flat under the load of incident light from the sun. Maintaining a flat shape is important to increase the propulsive action for solar sailing or the total absorption of concentrated photovoltaics.

It is well known that thin sheets can carry very little compression, making them susceptible to wrinkling. There is an extensive literature on statically loaded membranes, including many solution techniques that neglect the bending stiffness altogether. Tension field theory is the main analytical tool (Reissner, 1938; Mansfield, 1970, 1989; Pipkin, 1986) whereas numerical solutions were pursued by Stein and Hedgepeth (1961) and Miller and Hedgepeth (1982).

The bending stiffness of the membrane, which determines the wavelength of the wrinkles, was considered by several authors (Rimrott and Cvercko, 1986; Cerda et al., 2002; Epstein, 2003). The development of heavily wrinkled configurations, through jumps in which the spatial wavelength of the wrinkles changes suddenly, was studied by Wong & Pellegrino (2006a,b,c). There are also many applications in which membranes are loaded dynamically (Jenkins and Leonard, 1991).

The particular situation of interest in the present study is a spinning membrane, deformed out of plane by a transverse uniform loading. For small loads the structure deforms into an axisymmetric shallow "cone" and, at sufficiently

large transverse loads, it buckles into a wrinkled surface. A similar instability in statically loaded plates was studied by Keller & Reiss (1958) using the von Kármán plate equations, to illustrate a new iterative numerical method for certain boundary value problems in the nonlinear theory of thin plates and shells. The dynamic problem was first studied by Simmonds (1962), using a stress based wrinkling criterion that neglects the bending stiffness of the membrane. In this case, i.e., assuming zero bending stiffness, the onset of compression initiates wrinkling. Simmonds noted that, in a spinning membrane transversely loaded by gravity, circumferential compression first occurs on the outer edge. Hence, he evaluated the load at which the circumferential stress on the outer edge becomes negative, and assumed this load to be equal to the critical buckling load of the membrane. Okuizumi (2007) carried out experiments in a vacuum chamber on thin, spinning membranes loaded by gravity and vibrating under axisymmetric excitation (Okuizumi, 2009, 2014), using Simmonds' stress criterion to predict buckling.

Benson & Bogy (1978); Benson (1983); Cole & Benson (1988) studied the deflection of a floppy disk under a stationary, concentrated transverse load, including the coupling effects of bending stiffness and in-plane forces. Chen & Fang (2011) studied the buckling of a spinning heavy disk using the von Kármán plate equations to account for the bending stiffness and pre-stress due to centrifugal forces. Their analysis showed the existence of several equilibrium solutions. They theoretically and experimentally found the equilibrium shape of a rotating heavy disk and experimentally measured buckling wave numbers smaller than 4. These authors also analyzed the stability of rotating non-flat disks (Chen & Chang, 2007; Chen & Fang, 2010; Chen, 2010), however they did not provide a complete theoretical understanding of the buckling of flexible disks. For example, a "phase diagram" that clearly shows when the disk will and will not buckle would be very useful for a space structure designer. Also, the theoretical predictions in these previous studies were verified only qualitatively with experimental observations, and only up to mode numbers of 5 or 6. No detailed numerical simulations were carried out.

The present study considers circular, spinning membranes under a transverse, uniform load. No particular wrinkling criterion is assumed and both centrifugal forces and the effects of the membrane's bending stiffness are taken into account. The angular velocities and buckling (wrinkling) modes of membranes with different properties and geometries were measured experimentally, and buckling mode transitions were observed during spin down. The buckling problem is formulated analytically and a complete solution that provides the critical angular velocities and critical loads, as well as the buckled shapes of the spinning membrane, is obtained. The von Karman plate model is used to study buckling from the initial, axisymmetric configuration. A wide range of parameters is considered and a master curve that determines the stability of a membrane in terms of two non-dimensional parameters, namely the the equivalent gravity and the equivalent angular velocity, is obtained. It is also shown that the shape of the wrinkled membrane varies depending on the angular velocity, and the link between this result and the experimentally observed mode transitions is investigated. Comparison of the present results to the Simmonds theory shows that neglecting the bending stiffness of the membrane is inaccurate in certain regimes. Hence, the limit of validity of the pure membrane and static plate theories are established.

The first part of the paper presents the experimental setup for spinning membranes loaded by gravity, and presents specific results for three cases. Two analytical models are considered and compared, to explain these experimental observations, first a pure membrane model that neglects the bending stiffness and second a von Kármán plate formulation that includes both bending stiffness and in-plane stress due to centrifugal force. These models are used to evaluate the critical transverse load at any given angular velocity. For the latter model the corresponding wrinkling wave number is also obtained. An alternative, finite element simulation scheme is developed, to derive the buckling limit following a nonlinear loading path. A comparison of results from experiments, membrane and plate theories, and finite element simulations is presented in the form of a general stability chart, which identifies the stability limits in terms

of dimensionless parameters, for any membrane. Experimental measurements and numerical simulations for the wrinkling mode transitions that occur during spin down of a wrinkled membrane are presented. Finally, an application to a spinning solar power collecting membrane in space is described.

2. Experiments

2.1. Test Setup

An experimental setup that horizontally spins a membrane in a transparent vacuum chamber, at controlled angular velocities of up to 1200 rpm, was developed, as shown in Fig. 1. A uniform transverse load on the membrane was provided by Earth's gravity.

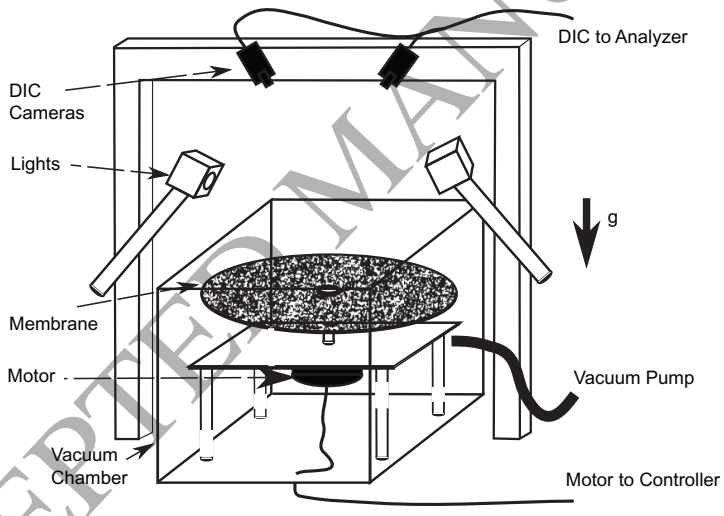

Figure 1: Schematic of test setup.

A flat, closed loop 90 Watt brushless motor with Hall sensors from Maxon, model EC 90, with an ESCON 50/5, 4-Q servocontroller was used. The motor voltage profile was prescribed though NI Signal Express and a digital-to-analog converter was used to input the profile to the controller. The rotation of the hub was measured and found to closely follow the imposed profile, see Fig. 3.

There were two main reasons for setting up the experiments inside a vacuum chamber. First, it is difficult to spin up the membrane in air as it tends to stick to the supporting plate. Second, the surrounding air would perturb the membrane equilibrium shape while the membrane is spinning, by dynamically exciting it and creating flutter instabilities. Use of a custom made, transparent acrylic chamber of size 125×10^3 cm^{-3} enabled illumination and imaging of the membrane from the outside.

The chamber was positioned on a thick aluminum plate with a central, sealed hole for the leads connecting the controller to the motor. A roughing pump from Welch provided a steady vacuum level of 0.03 atm, which is adequate to avoid flutter. Renshaw et al (1994) derived an analytical model to estimate the flutter limit for rotating disks in air, considering an infinite enclosure and a hub to membrane ratio of 0.3. Based on those estimates and considering the dimensions of the present experiments, flutter should theoretically be avoided even in the case of the thinnest membrane tested. In addition, buckling shapes are stationary (in the rotating frame) while flutter-induced vibration causes dynamic deflections. Hence, since all measurements of the membrane were in the same rotating frame of reference, it was confirmed that buckling shapes had been measured. The full setup is shown in Fig. 2.

Stereo Digital Image Correlation (DIC), as implemented by Correlated Solutions, was used to measure the equilibrium shapes of the membranes. The stereo DIC system consisted of two Point Grey Grasshopper cameras (GRAS-50S5M-C) with a resolution of 2448 $\times$ 2048, 3.45 μm pixel size and a gain range between 0 and 24 dB. The lenses had a focal length of 12 mm and the stereo angle was set at about 25°. The cameras were held 70 cm above the chamber to achieve the required field of view. The commercial software VIC-Snap was used to acquire synchronized images of the membrane, at a specified rate, and the software VIC-3D by Correlated Solutions was used to correlate the pairs of images. The largest membrane had a diameter of 40 cm and the field of view was about 50 cm, corresponding to a pixel size of 200 μm. The out-of-plane accuracy of the measurements can be estimated from the standard deviation

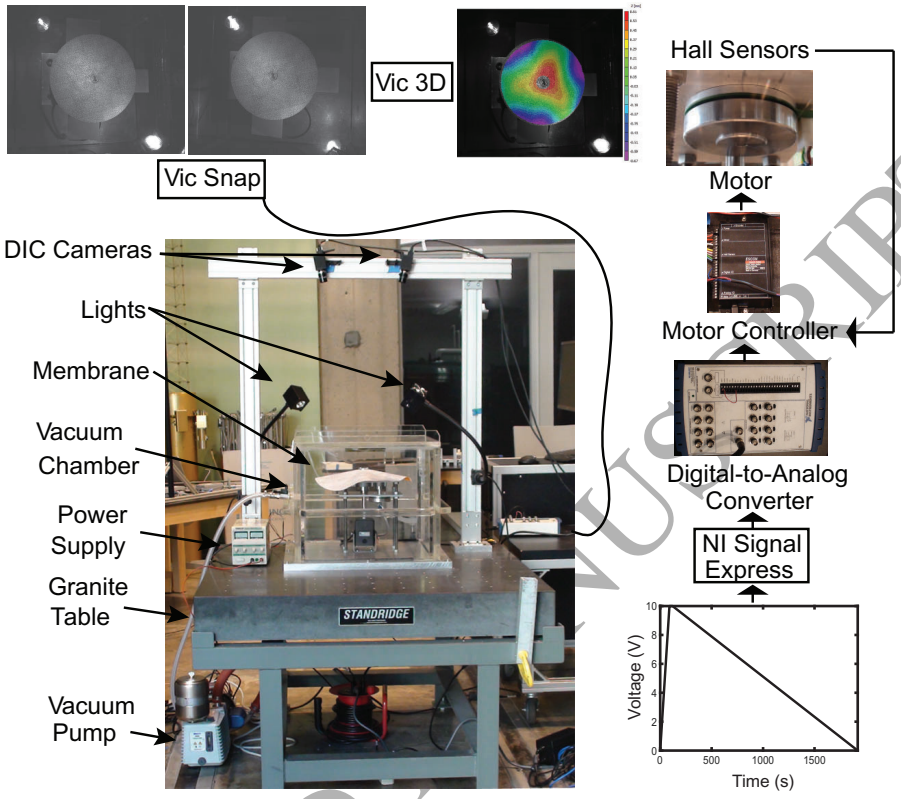

Figure 2: Full test setup starting from input voltage to motor controller, lower right, to measured 3D shape of spinning membrane, upper right.

value, 1σ, provided by Vic-3D. For all our measurements, $1\sigma < 0.04$ px which, taking into account the geometry of the setup, leads to an out-of-plane accuracy of about 40 μm. Note that this value is smaller than the smallest thickness of the test membranes.

2 mm wide (10 px) speckles were marked on the membrane with black ink and a roller rubber stamp after spraying the membrane with a thin layer of white paint. The paint thickness was 10 μm and its effect on the buckling limit of the thinnest Kapton membrane can be quantified by assuming the density of the paint to be equal to Kapton and its Young's modulus to be negligible in comparison to the Young's modulus of Kapton. Hence, modeling the painted

Kapton as a uniform isotropic membrane with a density of 1700 kg m^{-3} instead of the actual density of 1420 kg m^{-3}, the theory of Section 3 shows that the paint introduces an error of only 3% on the buckling speed and 5% on the wave number.

In DIC, choosing a larger subset decreases the noise but also decreases the spatial resolution of the measurement. Hence, a subset of 29 pixels (corresponding to a square with side length of 0.58 cm) and a density of 7 pixels were chosen, providing 51,372 measurement points overall, corresponding to a spatial resolution of about 5 mm. The software parameters were set to: linear shape functions within each subset, with Gaussian weights, 8-tap spline pixel interpolation, and zero-normalized square difference minimization algorithm.

At the maximum angular velocity of 1,200 rpm the edge velocity of the membrane is 25 m s^{-1}. To reduce blurring on the outer edge and achieve sub-pixel resolution, the exposure time was set at 13 μs, which corresponds to a motion of 160 μm (0.8 px) for the speckles on the edge of the membrane. With these settings, no blurring was noticeable in the images, although the measurement noise was greater at higher angular velocity and towards the edges of the membranes.

2.2. Results

Before starting an experiment, the membrane was attached at the center to a rigid hub connected to the motor. Under these static conditions, the membrane forms a smooth cylindrical shape resting on the plate supporting the motor. The test procedure consisted in spinning up the membrane to the maximum angular velocity (1200 rpm); at this speed all tested membranes had reached a fully axisymmetric shape. For the first two test samples (aluminum plates Al-13 and Al-20, see Table 1), the angular velocity was decreased in steps of 50 rpm. Pairs of images were taken with the DIC cameras, after waiting 1 min after each step, to allow for any transient dynamic effects to dissipate. This sequence was repeated until the shape was no longer axisymmetric. For the third test sample (Kapton membrane Ka-20, see Table 1) the angular velocity was decreased at a

uniform rate of 1 rpm s^{-1} and images were taken every 10 seconds (see Fig. 3).

Test membrane	Al-13	Al-20	Ka-20
Young's modulus E (GPa)	69	69	2.5
Poisson's ratio ν	0.34	0.34	0.34
Density ρ (kg m^{-3})	2700	2700	1420
Thickness h (μm)	152	152	50
Outer radius b (cm)	13	20	20
Inner radius a (cm)	1.3	2	2

Table 1: Properties and dimensions of three test membranes.

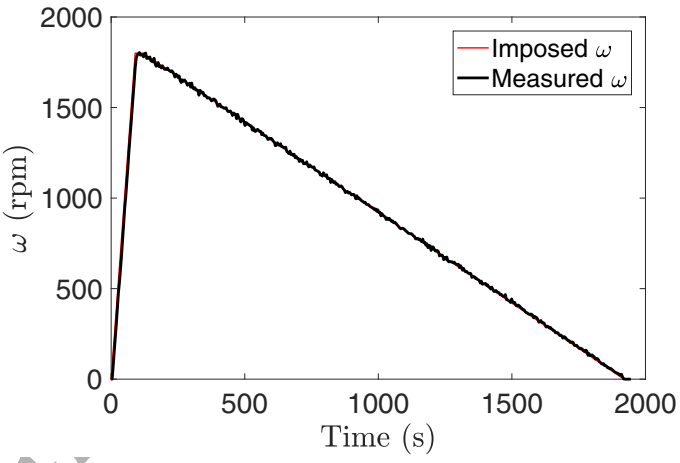

Figure 3: Measured angular velocity of motor axis (hub angular velocity is $\frac{2}{3}$ because of gears).

After completing these tests, the Vic3D software was used to obtain the shape of the membrane at each angular velocity, after removal of the rigid body components of the motion. For the aluminum membranes the wave number n was small and could be estimated directly from the images. For the membrane Ka-20, the experimentally obtained shapes were decomposed using the computed vibration mode shapes of the membrane as a basis. At all angular

velocities a significant $n = 0$ component was measured, corresponding to the axisymmetric, gravity induced deformation. Components in the range $n = 1, \ldots 6$ were considered to be due to the initial non-flatness of the membrane. In addition, only deflections larger than the thickness of each tested membrane were considered to be due to buckling, as smaller deflections were attributed to noise or imperfections. Thus, a membrane was considered to have buckled if a buckling mode shape with amplitude greater than h and $n \geq 6$ could be observed.

An analysis of the membrane shapes at each angular velocity showed that at a critical angular velocity the axisymmetric (pre-buckling) shape transitions to an n-fold symmetric buckled (wrinkled) shape. The wrinkling wave number n depends on the specific properties of the membrane. At lower angular velocities further transitions occur to buckled shapes with smaller values of n, as discussed in more detail in Section 5.

It will be shown in Section 3 that, for given Poisson's ratio and hub to outer radius ratio, this buckling problem is governed by two non-dimensional parameters: the equivalent gravity and the equivalent angular velocity. The three test membranes in Table 1 span a wide range of these two parameters; their axisymmetric, pre-buckling and buckled shapes are shown in Fig. 4. Note that the experimental pre-buckling shapes are not perfectly axisymmetric, due to geometric imperfections in the membranes.

Note that, due to imperfections and noise, several wave numbers can coexist in a measured buckled shape. In order to identify the dominant wave number, the measured shapes were decomposed using the computed vibration modes shapes of the membrane as a basis, as explained earlier. Figure 5 is a plot of the amplitude corresponding to each value of n for decreasing angular velocity, for the Kapton membrane. The critical velocities were found to be 1,100 rpm for Al-13, 800 rpm for Al-20, and 793 rpm for Ka-20. The wrinkling wave numbers, just after buckling, were $n = 3$ for Al-13, $n = 3$ for Al-20, and $n = 12$ for Ka-20.

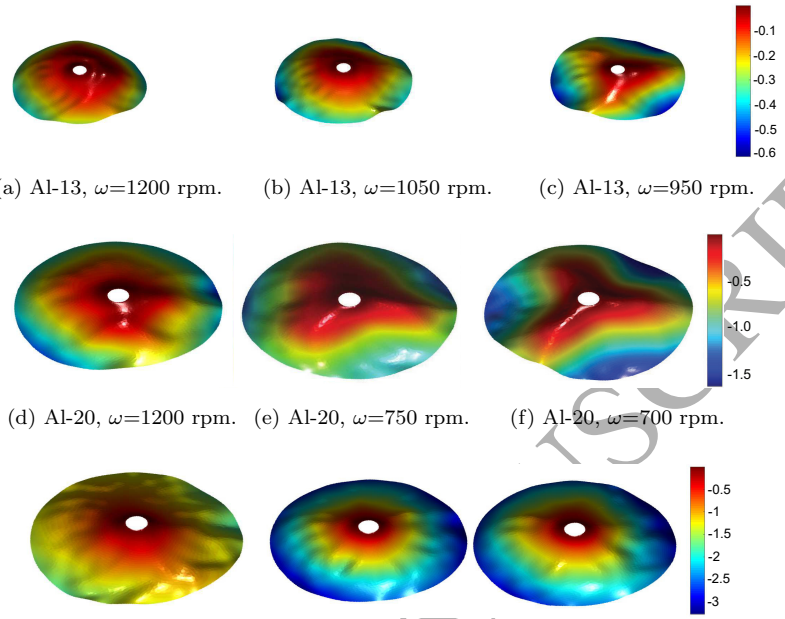

(a) Al-13, ω=1200 rpm. (b) Al-13, ω=1050 rpm. (c) Al-13, ω=950 rpm.

(d) Al-20, ω=1200 rpm. (e) Al-20, ω=750 rpm. (f) Al-20, ω=700 rpm.

(g) Ka-20, ω=1200 rpm. (h) Ka-20, ω=793 rpm. (i) Ka-20, ω=783 rpm.

Figure 4: Axisymmetric shapes (a, d, g), pre-buckling (b, e, h), and buckled (c,f,i) equilibrium shapes of tested membranes. Deflection units are mm.

3. Analytical Solutions

Consider an initially flat, circular membrane of uniform thickness h, outer radius b and attached at the center to a rigid, circular hub of radius a. The membrane has density ρ, Young's modulus E and Poisson's ratio ν. A polar coordinate system $\overline{r}, \theta$ is defined. The membrane is spun with angular velocity $\omega = \dot{\theta}$ around an axis perpendicular to the hub; a uniform distributed load q_0 is applied in the direction of the spin axis; the deflection component of the membrane in the axis direction is $\overline{w}$ at a radial distance $\overline{r}$, as shown in Fig. 6. q_0 corresponds to a normal pressure loading on the membrane, or it can represent a gravity loading $q_0 = \rho g h$ where g is the acceleration due to gravity.

Following Chen & Fang (2011), the following non-dimensional parameters

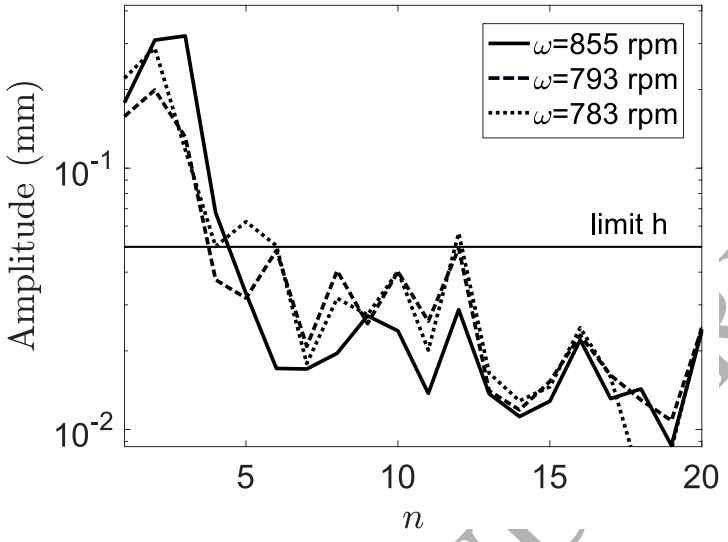

Figure 5: Experimentally derived wave numbers for Ka-20 test sample, at ω = 855, 793 , and 783 rpm. The horizontal line $h = 50$ μm indicates the membrane thickness.

are defined:

$$r = \frac{\bar{r}}{b} \qquad \alpha = \frac{a}{b}$$
$$w = \frac{\bar{w}}{h} \qquad \Phi = \frac{\bar{\Phi}}{D}$$
$$\Omega = \sqrt{\frac{\rho h}{D}} b^2 \omega \qquad G = \frac{b^4}{Dh} q_0 \tag{1}$$

where $D = Eh^3/12(1-\nu^2)$ is the flexural stiffness and Φ is a stress function.

Note that r, w, Φ with overbars are dimensional quantities, whereas the non-dimensional quantities without overbars will be used later in the analysis.

3.1. Membrane Theory

The membrane equations for a thin, spinning membrane (without any bending stiffness) under a transverse load were formulated by Simmonds (1962). Having defined the loading parameter:

$$k = \frac{16 E q_0^2}{(3+\nu)^3 h^2 \rho^3 b^4 \omega^6} \tag{2}$$

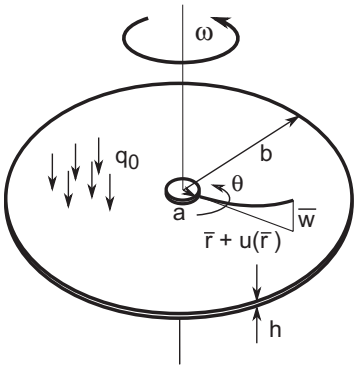

Figure 6: Definition of geometry and loading.

Simmonds assumed that wrinkling occurs when the circumferential stress on the outer edge transitions from tensile to compressive. He then showed that the critical value of k at which wrinkling occurs, k_{crit}, depends only on the non-dimensional outer radius α, and on the Poisson's ratio of the membrane. k_{crit} has been plotted in Fig. 7 and more details are provided in the Appendix.

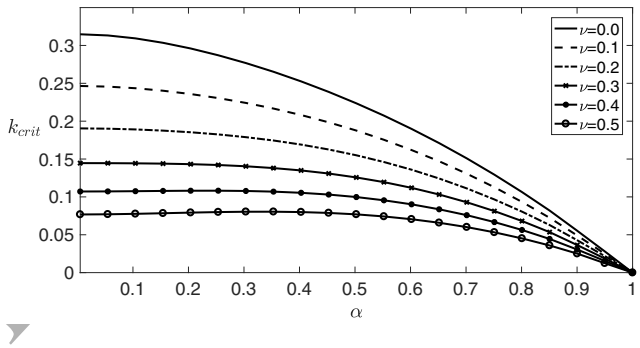

Figure 7: Variation of k_{crit} with α and ν.

Simmonds' result can be expressed in terms of the dimensionless parameters G and Ω defined in Eq. 1, and it can be shown that G is proportional to the

cube of Ω:

$$G = \sqrt{\frac{k_{crit}\left(\alpha,\nu\right)\left(3+\nu\right)^3}{192\left(1-\nu^2\right)}}\Omega^3 \tag{3}$$

3.2. Thin Plate Theory

A more detailed theory, first proposed by Nowinski (1964), includes the bending stiffness of the membrane and uses the von Kármán plate theory. In this theory, the stability of the deflected membrane is related to the positive definiteness of the stiffness operator. The membrane will buckle when at least one eigenvalue reaches zero and the wrinkling wave number corresponds to the waviness of the unstable mode.

The geometrically nonlinear axisymmetric equilibrium equations of a spinning plate, outlined in the next section, are perturbed to derive the eigenvalue problem that is then solved for increasing angular velocities, considering a wide range of gravity magnitude and a wide range of eigenmodes, until negative eigenvalues are obtained.

3.2.1. Nonlinear Equilibrium Equations

The governing equations for spinning membranes derived by Nowinski (1964) and later summarized by Nayfeh (2000) are as follows:

$$\begin{aligned}\rho h\frac{\partial^2\bar{w}}{\partial\bar{t}^2} + D\nabla^4\bar{w} + \frac{1}{2}\rho h\omega^2\bar{r}^2\nabla^2\bar{w} + \rho h\omega^2\bar{r}\frac{\partial\bar{w}}{\partial\bar{r}} = \\ \frac{\partial^2\bar{w}}{\partial\bar{r}^2}\left(\frac{1}{\bar{r}}\frac{\partial\bar{\Phi}}{\partial\bar{r}} + \frac{1}{\bar{r}^2}\frac{\partial^2\bar{\Phi}}{\partial\theta^2}\right) + \frac{\partial^2\bar{\Phi}}{\partial\bar{r}^2}\left(\frac{1}{\bar{r}}\frac{\partial\bar{w}}{\partial\bar{r}} + \frac{1}{\bar{r}^2}\frac{\partial^2\bar{w}}{\partial\theta^2}\right) \\ - 2\left(\frac{1}{\bar{r}}\frac{\partial^2\bar{\Phi}}{\partial\bar{r}\partial\theta} - \frac{1}{\bar{r}^2}\frac{\partial\bar{\Phi}}{\partial\theta}\right)\left(\frac{1}{\bar{r}}\frac{\partial^2\bar{w}}{\partial\bar{r}\partial\theta} - \frac{1}{\bar{r}^2}\frac{\partial\bar{w}}{\partial\theta}\right) + q_0\left(\bar{r},\theta,\bar{t}\right)\end{aligned} \tag{4}$$

$$\nabla^4\bar{\Phi} - 2\left(1-\nu\right)\rho h\omega^2 = Eh\left[\left(\frac{1}{\bar{r}}\frac{\partial^2\bar{w}}{\partial\bar{r}\partial\theta} - \frac{1}{\bar{r}^2}\frac{\partial\bar{w}}{\partial\theta}\right)^2 - \frac{\partial^2\bar{w}}{\partial\bar{r}^2}\left(\frac{1}{\bar{r}}\frac{\partial\bar{w}}{\partial\bar{r}} + \frac{1}{\bar{r}^2}\frac{\partial^2\bar{w}}{\partial\theta^2}\right)\right] \tag{5}$$

Here, the natural frequencies of the in-plane modes of vibration are assumed to be large compared to the frequencies of the transverse modes so that radial

and circumferential accelerations ($\frac{\partial^2 u}{\partial t^2}$ and $\frac{\partial^2 v}{\partial t^2}$) can be neglected. Also, the constant forcing term q_0 has been added to Nowinsky's equations.

The boundary conditions at the clamped edge are:

$$\bar{w} = 0,\ \frac{\partial \bar{w}}{\partial \bar{r}} = 0,\ u = 0, \text{ and } v = 0 \tag{6}$$

The mid-plane strains are related to the transverse displacement w, the radial displacement u, and the circumferential displacement v by:

$$e_r = \frac{\partial u}{\partial \bar{r}} + \frac{1}{2}\left(\frac{\partial \bar{w}}{\partial \bar{r}}\right)^2 \tag{7}$$

$$e_\theta = \frac{u}{\bar{r}} + \frac{1}{\bar{r}}\frac{\partial v}{\partial \theta} + \frac{1}{2\bar{r}^2}\left(\frac{\partial \bar{w}}{\partial \theta}\right)^2 \tag{8}$$

$$e_{r\theta} = \frac{1}{\bar{r}}\frac{\partial u}{\partial \theta} + \frac{\partial v}{\partial \bar{r}} - \frac{v}{\bar{r}} + \frac{1}{\bar{r}}\frac{\partial \bar{w}}{\partial \bar{r}}\frac{\partial \bar{w}}{\partial \theta} \tag{9}$$

It follows that:

$$e_\theta = 0, \text{ and } \frac{\partial}{\partial \bar{r}}\left(\bar{r} e_r\right) - e_r - \frac{\partial}{\partial \theta}\left(e_{r\theta}\right) = 0 \tag{10}$$

From Eq. 10 the following conditions on the displacements u, v are obtained, in terms of the stress function:

$$\begin{aligned} &\frac{\partial^2 \bar{\Phi}}{\partial \bar{r}^2} - \nu\left(\frac{1}{\bar{r}}\frac{\partial \bar{\Phi}}{\partial \bar{r}} + \frac{1}{\bar{r}^2}\frac{\partial^2 \bar{\Phi}}{\partial \theta^2}\right) - \frac{(1-\nu)}{2}\omega^2 \bar{r}^2 = 0 \\ &\frac{\partial^3 \bar{\Phi}}{\partial \bar{r}^3} + \frac{1}{\bar{r}}\frac{\partial^2 \bar{\Phi}}{\partial \bar{r}^2} - \frac{1}{\bar{r}^2}\frac{\partial \bar{\Phi}}{\partial \bar{r}} + \frac{2+\nu}{\bar{r}^2}\frac{\partial^3 \bar{\Phi}}{\partial \bar{r}\partial \theta^2} - \frac{3+\nu}{\bar{r}^3}\frac{\partial^2 \bar{\Phi}}{\partial \theta^2} \\ &\qquad - (1-\nu)\,\omega^2 \bar{r} = 0 \end{aligned} \tag{11}$$

At the free edge the boundary conditions are:

$$N_r = 0,\ N_{r\theta} = 0,\ M_r = 0, \text{ and } Q_r + \frac{1}{\bar{r}}\frac{\partial M_{r\theta}}{\partial \theta} = 0 \tag{12}$$

The in-plane forces are related to $\bar{\Phi}$ by:

$$N_r = \frac{1}{\bar{r}}\frac{\partial \bar{\Phi}}{\partial \bar{r}} + \frac{1}{\bar{r}^2}\frac{\partial^2 \bar{\Phi}}{\partial \theta^2} - \frac{1}{2}\rho h \omega^2 \bar{r}^2 \tag{13}$$

$$N_\theta = \frac{\partial^2 \bar{\Phi}}{\partial \bar{r}^2} - \frac{1}{2}\rho h \omega^2 \bar{r}^2 \tag{14}$$

$$N_{r\theta} = -\frac{1}{\bar{r}}\frac{\partial^2 \bar{\Phi}}{\partial \bar{r}\partial \theta} + \frac{1}{\bar{r}^2}\frac{\partial \bar{\Phi}}{\partial \theta} \tag{15}$$

The moments and traverse shear forces are related to w by:

$$M_r = -D\left(\frac{\partial^2 \bar{w}}{\partial \bar{r}^2} + \frac{\nu}{\bar{r}}\frac{\partial \bar{w}}{\partial \bar{r}} + \frac{\nu}{\bar{r}^2}\frac{\partial^2 \bar{w}}{\partial \theta^2}\right) \tag{16}$$

$$M_\theta = -D\left(\frac{1}{\bar{r}}\frac{\partial \bar{w}}{\partial \bar{r}} + \frac{1}{\bar{r}^2}\frac{\partial^2 \bar{w}}{\partial \theta^2} + \nu\frac{\partial^2 \bar{w}}{\partial \bar{r}^2}\right) \tag{17}$$

$$M_{r\theta} = -D\left(1-\nu\right)\left(\frac{1}{\bar{r}}\frac{\partial^2 \bar{w}}{\partial \bar{r}\partial \theta} - \frac{1}{\bar{r}^2}\frac{\partial \bar{w}}{\partial \theta}\right) \tag{18}$$

$$Q_r = -D\frac{\partial}{\partial \bar{r}}\left(\nabla^2 \bar{w}\right) \tag{19}$$

$$Q_\theta = -\frac{D}{\bar{r}}\frac{\partial}{\partial \theta}\left(\nabla^2 \bar{w}\right) \tag{20}$$

Combining Eqs 13, 15, 16, 18, and 19 with Eq 12 gives:

$$\begin{aligned}
\frac{\partial}{\partial \bar{r}}\left(\nabla^2 \bar{w}\right) + \frac{(1-\nu)}{\bar{r}^2}\frac{\partial^2}{\partial \theta^2}\left(\frac{\partial \bar{w}}{\partial \bar{r}} - \frac{\bar{w}}{\bar{r}}\right) &= 0 \\
\frac{\partial^2 \bar{w}}{\partial \bar{r}^2} + \nu\left(\frac{1}{\bar{r}}\frac{\partial \bar{w}}{\partial \bar{r}} + \frac{1}{\bar{r}^2}\frac{\partial^2 \bar{w}}{\partial \theta^2}\right) &= 0 \\
\frac{1}{\bar{r}}\frac{\partial \bar{\Phi}}{\partial \bar{r}} + \frac{1}{\bar{r}^2}\frac{\partial^2 \bar{\Phi}}{\partial \theta^2} - \frac{1}{2}\omega^2 \bar{r}^2 &= 0 \\
-\frac{1}{\bar{r}}\frac{\partial^2 \bar{\Phi}}{\partial \bar{r}\partial \theta} + \frac{1}{\bar{r}^2}\frac{\partial \bar{\Phi}}{\partial \theta} &= 0
\end{aligned} \tag{21}$$

Introducing the non-dimensional parameters in Eq. 1, Eqs 4 and 5 can be written in the form:

$$\begin{aligned}
\nabla^4 w_{eq} + \Omega^2\left(\frac{1}{2}r^2\nabla^2 w_{eq} + r\frac{\partial w_{eq}}{\partial r}\right) - L(w_{eq}, \Phi_{eq}) &= G \\
\nabla^4 \Phi_{eq} + 6\left(1-\nu^2\right)L(w_{eq}, w_{eq}) - 2\left(1-\nu\right)\Omega^2 &= 0
\end{aligned} \tag{22}$$

where the operator L is defined as:

$$\begin{aligned}
L(w,\Phi) = \frac{\partial^2 w}{\partial r^2}\left(\frac{1}{r}\frac{\partial \Phi}{\partial r} + \frac{1}{r^2}\frac{\partial^2 \Phi}{\partial \theta^2}\right) + \frac{\partial^2 \Phi}{\partial r^2}\left(\frac{1}{r}\frac{\partial w}{\partial r} + \frac{1}{r^2}\frac{\partial^2 w}{\partial \theta^2}\right) \\
- 2\left(\frac{1}{r}\frac{\partial^2 \Phi}{\partial r\partial \theta} - \frac{1}{r^2}\frac{\partial \Phi}{\partial \theta}\right)\left(\frac{1}{r}\frac{\partial^2 w}{\partial r\partial \theta} - \frac{1}{r^2}\frac{\partial w}{\partial \theta}\right)
\end{aligned} \tag{23}$$

The non-dimensional boundary conditions can be obtained from Eqs 6, 11, and 21, by replacing ω by its dimensionless expression Ω.

The axisymmetric equilibrium shape of the membrane can be obtained from a subset of the above equations. The fourth equation in Eq. 21 is identically

satisfied and can be neglected. The remaining Eqs 21 - 22 define a boundary value problem consisting of two coupled 4th order ODEs that can be solved in Matlab using the built-in function bvp4c.

3.2.2. Buckling Equations

To derive the eigenvalue problem, a small perturbation (buckling mode), w, from the axisymmetric equilibrium configuration is considered. Substituting this perturbation into Eq. 22 and linearizing provides the stiffness operator near the axisymmetric equilibrium. The eigenvalues λ and eigenmodes (w,Φ) of the stiffness operator are the solutions of the boundary value problem:

$$\begin{aligned} -\lambda w + \nabla^4 w + \Omega^2 \left(\frac{1}{2} r^2 \nabla^2 w + r \frac{\partial w}{\partial r} \right) \\ = L(w, \Phi_{eq}(G,\Omega)) + L(w_{eq}(G,\Omega), \Phi) \\ \nabla^4 \Phi = -12 \left(1-\nu^2\right) L(w_{eq}(G,\Omega), w) \end{aligned} \tag{24}$$

The boundary conditions for the buckling mode are the same as the conditions on w_{eq} in Eqs 6 - 21, only replacing Ω with zero. Note that this approach is different than that of Chen & Fang (2011), where the centrifugal effect was separated from the main equation (see Eq. 17 of Chen & Fang (2011)).

The buckling modes are expressed by separation of variables:

$$\begin{aligned} w(r,\theta) &= W(r) \exp(in\theta) \\ \Phi(r,\theta) &= \Phi(r) \exp(in\theta) \end{aligned} \tag{25}$$

where n is an integer (due to periodicity in θ) and i the imaginary unit. The mode shapes end up being real valued.

3.3. Results

When G is increased, the edge displacement provided by the axisymmetric solution increases nonlinearly up to buckling. Its variation for $\Omega = 200$ has been plotted in Fig. 8a. The variation in the critical edge deflection on the point of buckling, for increasing Ω, has been plotted in Fig. 8b. Note that the trend of

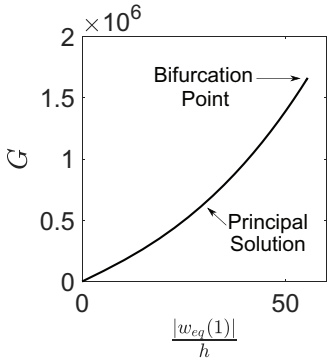

(a) Nonlinear loading path for Ω=200.

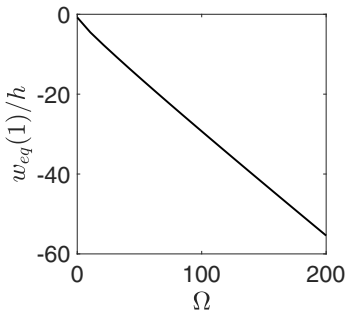

(b) Pre-buckling edge deflection.

Figure 8: Axisymmetric equilibrium of spinning membranes.

$w_{eq}(1)$ is close to linear, but the deflection at $\Omega = 0$ (static circular plate) is $0.80h$, whereas at $\Omega = 200$ its value is $55h$.

For membranes with given values of α and ν, and for $\Omega = 64$, the eigenvalues were computed for increasing G until the lowest eigenvalue became equal to zero, thus defining the condition $G = G_{crit}$. The same Matlab function bvp4c was used but this time an initial guess for both the shape function and the eigenvalue, and an additional boundary condition on the shape function ($W(1) = 1$, for example) had to be provided. The results from the previous increment in G were used as initial guess for the next increment.

The variation of the eigenvalues for increasing values of G has been plotted in

Fig. 9 for modes with one nodal circle and several values of n. In this example, the membrane geometry was set to $\alpha = 0.1$, the Poisson's ratio to $\nu = 0.34$ and the angular velocity to $\Omega = 64$.

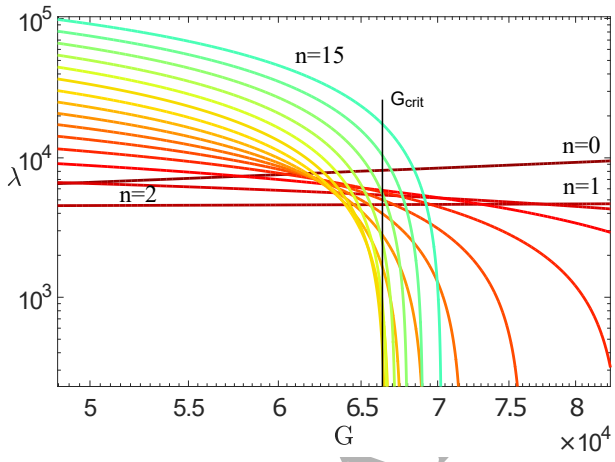

Figure 9: Variation of eigenvalues with G, for Ω=64, α=0.1, and ν=0.34. Note that $G_{crit} = 6.6 \times 10^4$ and $n_{crit} = 10$.

In this figure, note that the eigenvalues corresponding to $n = 0, 1$ increase monotonically with Ω: these eigenvalues never become zero. For all other modes, the corresponding eigenvalue reaches zero at some value of G, hence providing the buckling load associated with that particular value of n. For each value of Ω, the critical value of G corresponds to the lowest intersection with the axis $\lambda = 0$. Specifically, $G_{crit} = 6.6 \times 10^4$ and $n_{crit} = 10$.

Figure 10 shows the two additional cases $\Omega = 0$, $G_{crit} = 40$ and $n = 2$; and $\Omega = 200$, $G_{crit} = 1.6 \times 10^6$ and $n = 22$. Note that for larger Ω's the critical wave number occurs when there is an inversion in the trend of G for increasing n.

The critical wave numbers for two particular membrane geometries, $\alpha = 0.1, 0.7$ (with $\nu = 0.34$), spinning at increasing angular velocities have been plotted in Fig. 11, together with the corresponding buckling mode shape. Note that the waviness of the critical buckling mode increases with increasing Ω.

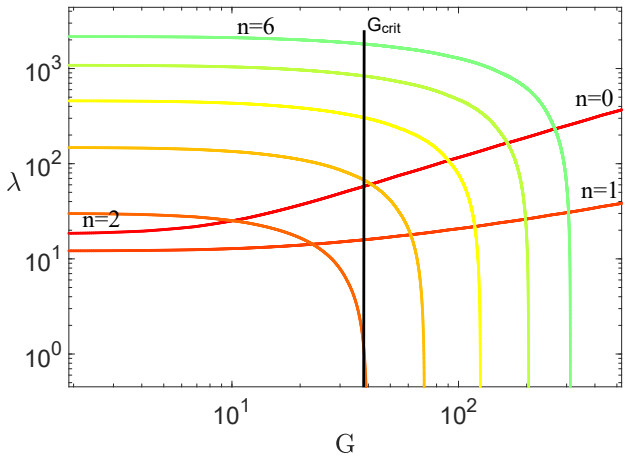

(a) Eigenvalues for Ω=0.

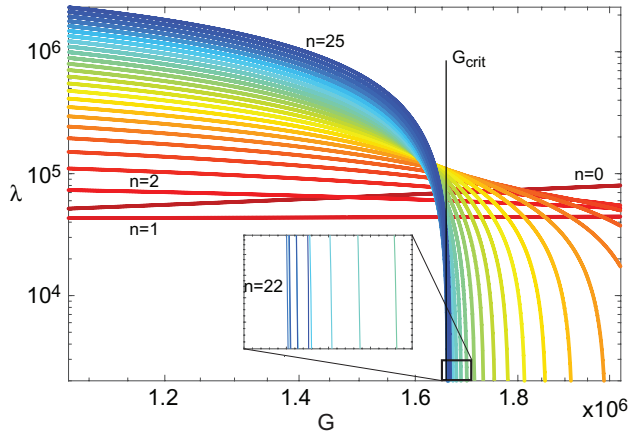

(b) Eigenvalues for Ω=200.

Figure 10: Eigenvalue variation for different eigenmodes.

3.4. Parametric Analysis

Results for a wide range of Ω and G but fixed α and ν have been presented already. This section studies the influence of α and ν on the stability of spinning membranes.

The finite element software Abaqus/Standard was used for this analysis.

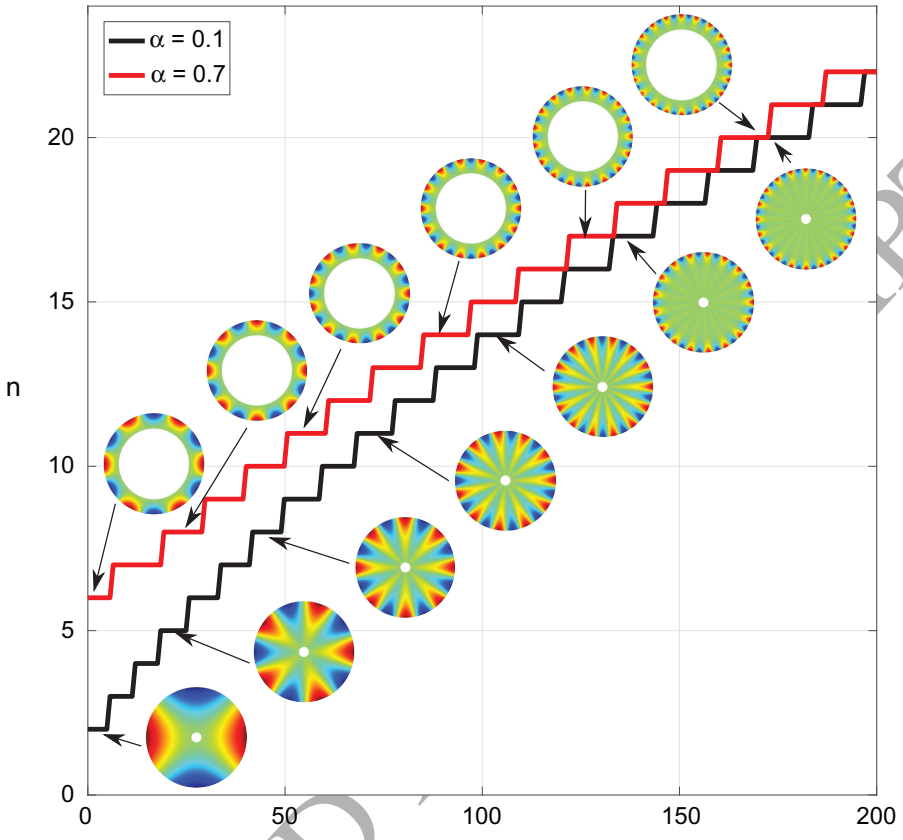

Figure 11: Variation of critical mode wave number and mode shapes with normalized angular velocity, for $\nu = 0.34$, and for α=0.1, and $\alpha = 0.7$.

Instead of choosing the built-in buckling option, which provides a linear perturbation analysis that however does not account for nonlinearity of the loading path, a Python script was written to compute the critical loads and wave numbers for a wide range of values of G and Ω.

The membrane was modeled as a linear elastic material with the properties of Kapton film, simulated with S4R elements: 4-node doubly curved thin shell elements with reduced integration, hourglass control, finite membrane strains, and 5 integration points through the thickness. These shell elements are numerically efficient, and based on the Kirchhoff shell theory. The central hub

was modeled by rigidly constraining the nodes along the inner edge of the membrane. It is important to define a fine mesh along the outer edge, as wrinkling is triggered by compression along this edge and an insufficiently fine mesh could cause the wrinkles to become localized. Hence, a dense mesh was defined, with 1000 nodes on the outer edge and 1000α on the inner edge. The simulation was run in two steps. First, a nonlinear static step, to evaluate the axisymmetric equilibrium of the membrane under centrifugal forces and gravity. Second, a frequency analysis, to determine the gravity load that leads to the first zero eigenvalue for each Ω. A secant method algorithm was used. Ω was increased in small increments and the results of the previous Ω were used as initial guess for the next search. A similar technique would be suitable to estimate the buckling load for any problem that involves a nonlinear loading path.

The wrinkle wave number was automatically computed using the Fourier transform of the outer edge deflection. The results from this analysis and the previous Matlab solution were compared for the case α=0.1 and ν=0.34 and gave the exact same results over the full range Ω=[0...200].

The master curves shown in Fig. 12 were obtained by running the Python script. Figure 12a and Fig. 12b show the influence of α (for ν=0.34) and ν for (α=0.1) on G_{crit}. They show that ν has little influence on the critical load, while increasing α has the effect of increasing G_{crit} for given Ω, or decreasing Ω_{crit} for given G. Figure 12c shows that increasing α at constant ν has the effect of increasing the wave number as well, but at higher Ω this effect tends to disappear. Figure 12d shows the influence of ν on the critical wave number, for the case α=0.1. It shows that increasing the Poisson's ratio ν has the effect of increasing the wave number, for a given Ω.

3.5. Discussion

A physical interpretation of the buckling behavior of thin membranes can be obtained from simple energy arguments. Consider a rigid bar pinned at the top and loaded by gravity. If the support rotates at uniform angular velocity about a vertical axis, the bar is in equilibrium at an angle to the vertical. The

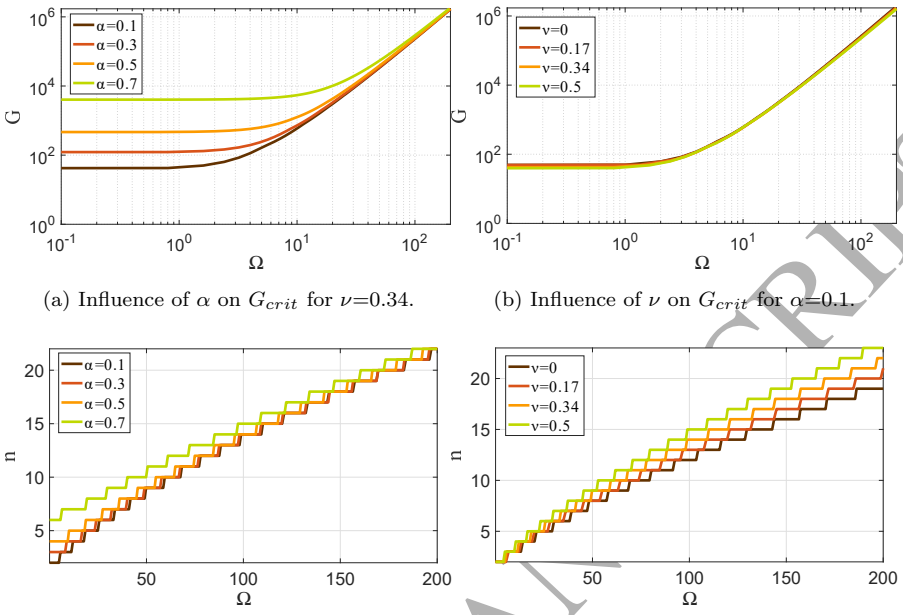

(a) Influence of α on G_{crit} for ν=0.34.

(b) Influence of ν on G_{crit} for α=0.1.

(c) Influence of α on n_{crit} for ν=0.34.

(d) Influence of ν on n_{crit} for α=0.1.

Figure 12: Variation of critical loads (G,Ω) and wrinkling wave number, with α for ν=0.34, and with ν for α=0.1 .

value of this angle is determined by the balance between gravity and centrifugal (D'Alembert) forces. Next, consider a thin circular membrane, held at the center and spinning around a vertical axis through this point. In analogy to the rigid bar, it wants to take up an axisymmetric, near-conical configuration, which provides stationary potential energy due to centrifugal force and gravity. This configuration requires the outer perimeter of the membrane to become shorter, and this shortening induces in-plane strain energy in the membrane. When this energy is too high, the membrane can find an alternative equilibrium shape around the cone, by creating a wavy configuration with lower energy. When the membrane is thin the centrifugal force also creates a tensioning hoop stress that releases some of the compression induced by the cone deflection. This means that at high Ω we expect higher deflection before buckling, as confirmed by Fig. 8b. The waves in the buckled configuration increase the bending energy

of the membrane while releasing some of the in-plane energy associated with shortening the outer perimeter. Because the bending energy of the wrinkled membrane increases with both bending stiffness and wave number, membranes with higher bending stiffness need fewer waves to achieve the same amount of internal energy, which explains why at lower Ω the wave number is smaller.

In Fig. 9, it is important to note that close to G_{crit} the eigenvalue vs. loading curves become tightly bunched and hence there are many values of n within a small range of G_{crit}. Therefore, it can be expected that it will be difficult to observe experimentally the predicted buckling mode.

4. Comparison of Plate Theory with Membrane Theory, Finite Element Simulations, and Experiments

Figure 13 shows a comparison of the results from the present theory with the membrane theory by Simmonds (1962), with nonlinear finite element simulations, and with the experimental results presented in Section 2. According to pure membrane theory, G_{crit} is proportional to Ω^3, and the coefficient of proportionality decreases with both α and ν (Eq. 3). This theory does not resolve the waviness of the wrinkled mode shape. Figure 13 shows that the two theories converge at high values of Ω, which is to be expected since the effect of the bending stiffness of the membrane tends to become negligible.

Nonlinear static finite element simulations similar to the simulations described in Section 3.4 were carried out. For each angular velocity the critical load was estimated in two steps. First, a centrifugal force was statically applied to the membrane. Then, a gravity load was added in small increments, in a second static step. The membrane was assumed to have buckled once the amplitude of its outer edge waviness became greater than twice the thickness h of the membrane. The results of this analysis have been plotted with black hollow circles in Fig. 13, and they practically coincide with the results from the plate theory, across the full range of Ω. It is interesting to note that even if the von Kármán equations are an approximation to the three-dimensional nonlin-

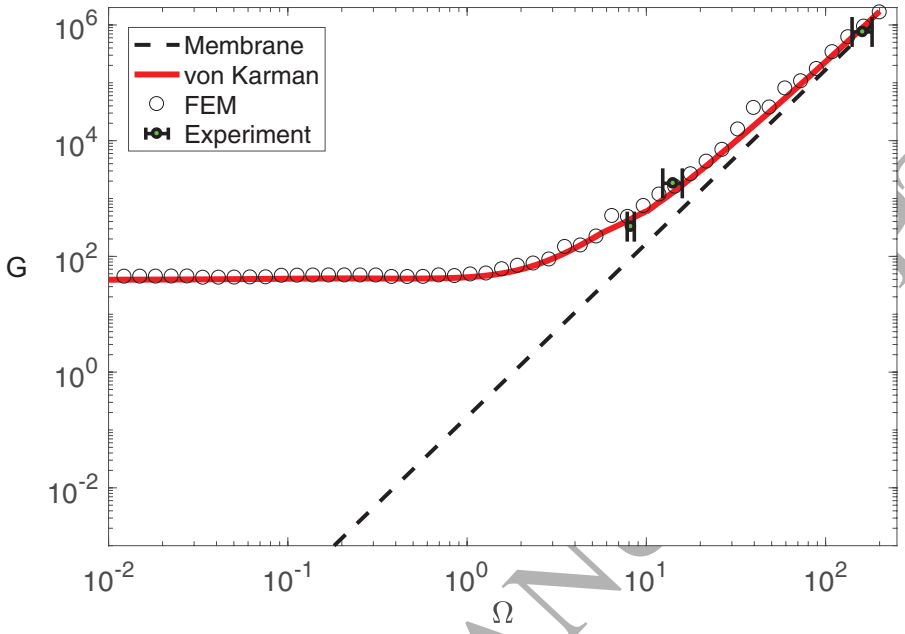

Figure 13: Comparison between buckling theory, membrane theory, finite element simulations and experiments.

ear elastic model, and are normally assumed to be valid for deflections limited to the plate thickness, in the present case they give excellent results for much larger deflections. For $\Omega = 10,\ 200$ the edge deflections just before buckling are respectively $4.5h$, $55\ h$.

Also plotted, in green in Fig. 13, are the critical pairs (G, Ω) for the three experiments presented in Section 2. These results are also in excellent agreement with the critical angular velocities from the plate theory. However, the theoretical buckling wave numbers are 3, 4, and 18 respectively for Al-13, Al-20, and Ka-20, whereas the experiments gave the values 3, 3, and 12 (see Table 2). As noticed in Section 3.5, the buckling limits tend to become quite close at higher values of Ω, and it is conjectured that this effect, in combination with initial curvature of the Kapton membrane, may explain why the theoretically obtained wave number is less accurate for the dimensions of the membrane Ka-20.

Test membrane	Al-13	Al-20	Ka-20
n experiment	3	3	12
n theory	3	4	18
ω_{crit} experiment (rpm)	1100	800	783
ω_{crit} Abaqus (rpm)	1050	921	730

Table 2: Comparison between experiments and theory.

5. Buckling Mode Transitions During Spin Down

A more detailed study was carried out of the experimentally observed changes in wrinkled shapes when the angular velocity is decreased below the critical angular velocity.

A range of selected shapes observed in the experiments is shown in Fig. 14.

A numerical simulation of the spin-down process for the membrane Ka-20, assumed to be initially flat, was performed with Abaqus/Standard. The finite element model was similar to the one described in Section 3.4, but this time an Euler-Backward integration scheme was used to compute quasi-statically the changes in the shape of the membrane as the centrifugal loading was decreased to simulate the membrane spin down. The accelerations due to changes in angular velocity and Coriolis effects were neglected. The simulation was performed in three steps. First, the centrifugal forces corresponding to a spin rate of 1000 rpm, were applied in a single, nonlinear static step. Once the membrane had become stiff enough to sustain gravity, a gravity acceleration of amplitude 9.81 m s^{-2} was applied in a nonlinear static step. Finally, the centrifugal forces were linearly decreased to zero, in increments corresponding to angular velocity changes of 0.5 rpm. Three computed equilibrium shapes are shown in Fig. 15.

A comparison of simulation results and experiments, for the membrane Ka-20, is presented in Fig. 16 (red and yellow plots, respectively). Although there is a significant difference in the initial buckling mode wave number for this membrane, as already noticed in Section 4, it is interesting to note that the

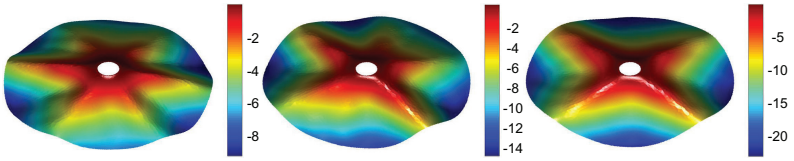

(a) Ka-20, ω=356 rpm. (b) Ka-20, ω=289 rpm. (c) Ka-20, ω=230 rpm.

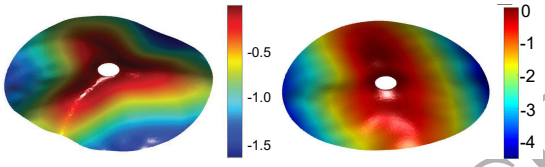

(d) Al-20, ω=700 rpm. (e) Al-20, ω=255 rpm.

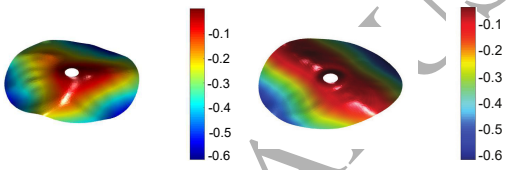

(f) Al-13, ω=950 rpm. (g) Al-13, ω=650 rpm.

Figure 14: Selected spin-down shapes of test membranes. Deflection units are mm.

wave numbers predicted by the simulation decrease rather rapidly, and become quite close to the experimentally observed trend for $\omega < 600$ rpm.

The numerical simulation of the actual spin down of membrane Ka-20 has been compared to the plate buckling theory. As the theory only describes the first transition from axisymmetric to wavy shape, one can only compare the first critical angular velocity (i.e. the highest angular velocity at which the membrane loses its axisymmetric shape) and the waviness of the first buckled shape during the simulated spin down. The comparison shows that buckling happens at 727 rpm and n=18. These values are very close to the theoretical values of 736 rpm and n=18, and thus there is an excellent match between theory and numerical simulations. Also note that the remaining buckling mode transitions do not match. An analysis of these mode transitions was carried out by Chen & Fang (2011).

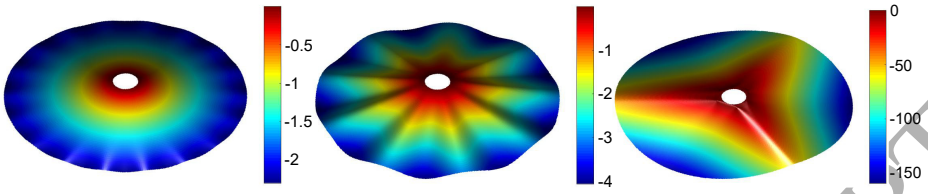

(a) Ω= 707 rpm. (b) Ω= 525 rpm. (c) Ω= 0 rpm.

Figure 15: Selected post buckling equilibrium shapes of membrane Ka-20. Deflection units are mm.

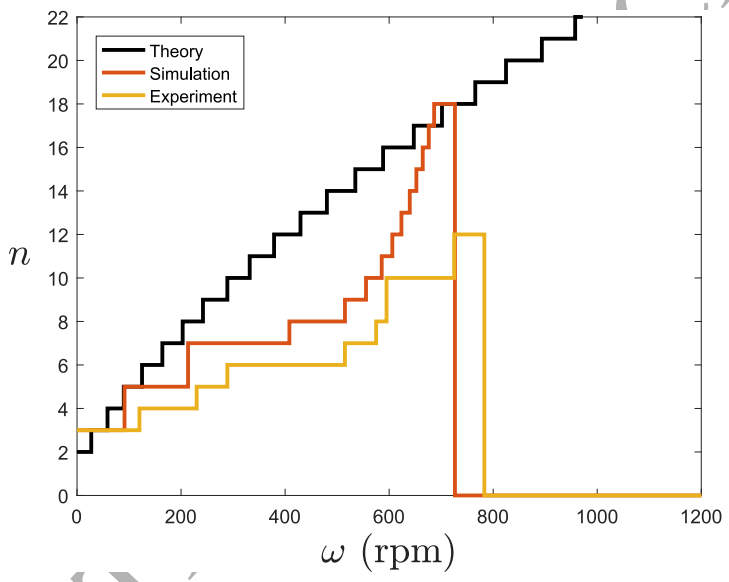

Figure 16: Comparison of mode shape wave number predicted by plate theory, with mode transitions from spin down experiments and numerical simulations, for membrane Ka-20.

6. Application to Spinning Spacecraft

Consider a circular membrane with a perfectly absorbent surface, spinning in geostationary orbit and pointed to the sun. It provides an ideal photovoltaic surface to gather solar energy.

Its radius is $r = 10$ m, the thickness $h = 100$ μm, and the Young's modulus and Poisson's ratio are identical to Kapton (see Table 1). This choice is made for simplicity, since the photovoltaic material has not been specified. The

magnitude of the solar pressure in geostationary orbit is $q_0 = 4.57 \times 10^{-6}$ Pa.

For these properties, $G = 1.2 \times 10^5$ and then the minimum non-dimensional rotation speed to avoid buckling is Ω_{crit}=79, obtained from Fig. 13. This value corresponds to $\omega = 1.3$ rpm.

7. Conclusion

Transverse uniform body forces acting on a spinning membrane induce deflections much greater than the membrane thickness, and these deflections result in compressive hoop stresses around the edge of the membrane. These stresses can buckle the membrane, forming a series of azimuthal wrinkles.

A general formulation of the problem has been presented, in terms of the dimensionless load G and dimensionless angular velocity Ω, defined in Eq. 1, and the critical values of G and Ω have been plotted in Fig. 13. For $\Omega < 1$, G_{crit} depends only on the bending stiffness of the membrane (bending dominated behavior), and hence it is constant with G. For $\Omega > 10$, the results of the membrane theory are recovered, confirming that wrinkling depends only on the mid-plane stress, and hence G increases with the cube of Ω (in-plane dominated behavior). Both of these specific numerical limits increase if the ratio between inner and outer radius of the membrane, α, is increased. Figure 13 is a useful chart from which one can determine the critical values of G and Ω, and also if buckling is governed by membrane or flexural behavior. If buckling is governed by flexural behavior, G is independent of Ω.

The buckling eigenvalues and the corresponding eigenmodes of the spinning membrane have been plotted for a specific value of Ω in Fig. 9. The figure shows that all eigenvalues for $n \geq 2$ decrease when Ω increases. The wrinkling mode of the membrane is determined by the eigenvalue that reaches zero first. The variation of the azimuthal wave number of the critical buckling mode for a specific value of Ω has been plotted in Fig. 11. It has been observed, both in experiments and through numerical simulations, that the wrinkling mode changes during spin down of the membrane. This behavior, plotted in Fig. 16,

qualitatively resembles the critical mode variation corresponding to different Ω.

APPENDIX

Following Simmonds (1962), k_{crit} can be obtained by solving a boundary value problem of the second-order ODE

$$\frac{d^2 f}{d\xi^2} + \left[\frac{k\,(1-\xi)^2}{f^2}\right] + 2 = 0 \tag{26}$$

with boundary conditions

$$f(1) = 0 \tag{27}$$

$$f(\alpha) - \frac{2\alpha^2}{1+\nu}\left(\frac{df}{d\xi}\Big|_{\xi=\alpha} + \frac{4\alpha^2}{3+\nu}\right) = 0 \tag{28}$$

The ODE is solved for increasing values of k, until the wrinkling criterion

$$2\frac{df}{dr}\Big|_{r=1} + \frac{8}{3+\nu} = 0 \tag{29}$$

is satisfied.

Acknowledgments

MD and SP acknowledge financial support from the Northrop Grumman Corporation.

References

References

Benson, R., 1983. Observation on the steady-state solution of an extremely flexible spinning disk with a transverse load. *Journal of Applied Mechanics*, **50**, 525–530.

Benson, R., & Bogy, D., 1978. Deflection of a very flexible spinning disk due to a stationary transverse load. *Transactions of ASME*, **45**, 636–642.

Cerda, E., Ravi-Chandar, K., Mahadevan, L., 2002. Wrinkling of an elastic sheet under tension. *Nature*, **419**, 579–580.

Chen, J., 2010. On the linearization of the equations of motion of a rotating disk. *Applied Mathematical Modelling*, **35**, 392–397.

Chen, J., & Chang, Y.-Y., 2007. On the unsymmetrical deformation and reverse snapping of a spinning non-flat disk. *Journal of Non-Linear Mechanics*, **42** , 1000–1009.

Chen, J., & Fang, Y., 2011. Warping of stationary and rotating heavy disks. *International Journal of Solids and Structures*, **48**, 3032–3040.

Chen, J., & Fang, Y.-Y., 2010. Non-axisymmetric warping of a heavy circular plate on a flexible ring support. *International Journal of Solids and Structures*, **47**, 2767–2774.

Clampin, M., 2008. Status of the James Webb Space Telescope (JWST). *Proceedings of SPIE, Space Telescopes and Instrumentation 2008: Optical, Infrared, and Millimeter*.

Cole, K., & Benson, R., 1988. A fast eigenfunction approach for computing spinning disk deflections. *Journal of Applied Mechanics*, **54** , 453–456.

Epstein, M., 2003. Differential equation for the amplitude of wrinkles. *AIAA Journal*, **41**, 327–329.

Jenkins, C. and Leonard, J.W., 1991. Nonlinear dynamic response of membranes: State of the art. *ASME Applied Mech. Reviews*, **44**, 319–328.

Keller, H. B., & Reiss, E. L., 1958. Non-linear bending and buckling of circular plates. *AEC Research and Development Report*.

Mansfield, E.H., 1989. *The bending and stretching of plates*, Second Edition. Cambridge University Press.

Mansfield, E.H., 1970. Load transfer via a wrinkled membrane. *Proc. R. Soc. Lond. A.*, **316**, 269–289.

Miller, R.K. and Hedgepeth, J.M., 1982. An algorithm for finite element analysis of partly wrinkled membranes. *AIAA Journal*, **20**, 1761–1763.

Nayfeh, A. H., 2000. *Nonlinear Interations:Analytical,Computational, and Experimental Methods*. Wiley, New York.

Nowinski, J. L., 1964. Nonlinear transverse vibrations of a spinning disk. *Journal of Applied Mechanics*, **31** , March, 72–78.

Okuizumi, N., 2007. Equilibrium of a rotating circular membrane under transverse distributed load. *Journal of System Design and Dynamics*, **1**, 85–95.

Okuizumi, N., 2009. Vibration mode analysis of a rotating circular membrane under transverse distributed load. *Journal of Design and Dynamics*, **3**, 95–105.

Okuizumi, N., 2014. Forced vibration experiments of a rotating extremely thin circular membrane. *Mechanical Engineering Journal*, **1**, No. 5, DR0054.

Pipkin, A.C., 1986. The relaxed energy density for isotropic elastic membranes. *IMA Journal Applied Mathematics*, **36**, 85–99.

Reissner, E., 1938. On tension field theory. *Proceedings 5th International Congress of Applied Mechanics*, 88–92.

Renshaw, A.A., D'Angelo III, C., and Mote, Jr, C.D., 1994. Aerodynamically excited vibration of a rotating disk. *Journal of Sound and Vibration*, **117**, 5, 577-590.

Rimrott, F.P.J., Cvercko, M., 1986. Wrinkling in thin plates due to in-plane body forces. In: *Inelastic behaviour of plates and shells*, (Edited by L. Bevilacqua, R. Feijoo and R. Valid), 19–48. Springer-Verlag.

Satou, Y., Mori, O., Okuizumi, N., Shirasawa, Y., Furuya, H., & Sakamoto, H., 2015. Deformation properties of solar sail IKAROS membrane with nonlinear finite element analysis. *2nd AIAA Spacecraft Structures Conference*.

Sawada, H., Mori, O., Okuizumi, N., Shirasawa, Y., Miyazaki, Y., Natori, M., Matunaga, S., Furuya, H., & Sakamoto, H., 2007. Mission report on the solar power sail deployment demonstration of IKAROS. *52nd AIAA/ASME/ASCE/AHS/ASC Structures, Structural Dynamics and Materials Conference*.

Simmonds, J., 1962. The finite deflection of a normally loaded, spinning, elastic membrane. *Journal of Aerospace Sciences*, **29**, 16–18.

Steigmann, D.J., 1990. Tension Field Theory. *Proceedings of the Royal Society of London Part A*, **429**, 141–173.

Stein, M., Hedgepeth, J.M., 1961. Analysis of partly wrinkled membranes. NASA Langley Research Center, NASA TN D-813.

Wong, Y. W., & Pellegrino, S., 2006 a. Wrinkled membranes part I: experiments. *Journal of Mechanics of Materials and Structures*, **1**, 3–25, doi: 10.2140/jomms.2006.1.3.

Wong, Y. W., & Pellegrino, S., 2006b. Wrinkled membranes part II: analytical models. *Journal of Mechanics of Materials and Structures*, **1**, 27–61, doi:10.2140/jomms.2006.1.27.

Wong, Y. W., & Pellegrino, S., 2006c. Wrinkled membranes part III: numerical simulations. *Journal of Mechanics of Materials and Structures*, **1**, 63–95, doi: 10.2140/jomms.2006.1.63.